4. Study of Fast ion Transport by TAE

4.1 Introduction

In the burning plasma with a high alpha particle pressure gradient, Alfvén eigenmode (AE) can be destabilized by alpha particles. This destabilized AE can induce the enhanced transport of alpha particles from the core region and can cause the degradation of the performance of a fusion reactor. Loss of alpha-particles may also damage the first wall[1]. Therefore the understanding of the alpha particle transport when AEs are destabilized is important. The AE experiments have been performed in several Tokamaks. So far, however, only a limited parameter domain in the $v_{b//}/v_A$ (the ratio of parallel beam ion velocity to the Alfvén velocity) and $\langle\beta_h\rangle$ (volume averaged hot ion β) space has been studied. Toroidicity-induced Alfvén eigenmode (TAE) experiments by α-particles in TFTR were mostly performed with low $\langle\beta_h\rangle$. While, at high $\langle\beta_h\rangle$, chirping modes were observed in DIII-D[2] as shown in Fig.1.1.

In JT-60U, the regime of $0.1\% < \langle\beta_h\rangle < 1\%$ and $v_{b//}/v_A \sim 1$ has been covered recently with the Negative-ion-based Neutral Beam (N-NB) of $E_{beam} \geq 360$ keV in order to assess the AE activity and the effect of AEs on the loss of energetic ions in the ITER relevant domain [3]. In the N-NB injection experiments, the birth domain of the ITER alhpa particles can be explored. Thus, experiments which simulated the operation condition of burning plasma in/near ITER become possible.

4.1.1 Recent result of Alfvén eigenmode experiments using NNB in JT-60U

Typical time trace of plasma parameters and a frequency spectrum of magnetic fluctuations by magnetic probe of an AE experiment using N-NB are shown in Fig.4.1. We can see several types of modes. Magnetic fluctuations with large frequency sweeping were observed from t = 3.8s and subsequently the frequency saturated at about 4s. We label this type of instability as a "slow frequency sweeping (Slow FS) mode". After 4.1s, instabilities with faster chirping mode (Fast FS mode) start

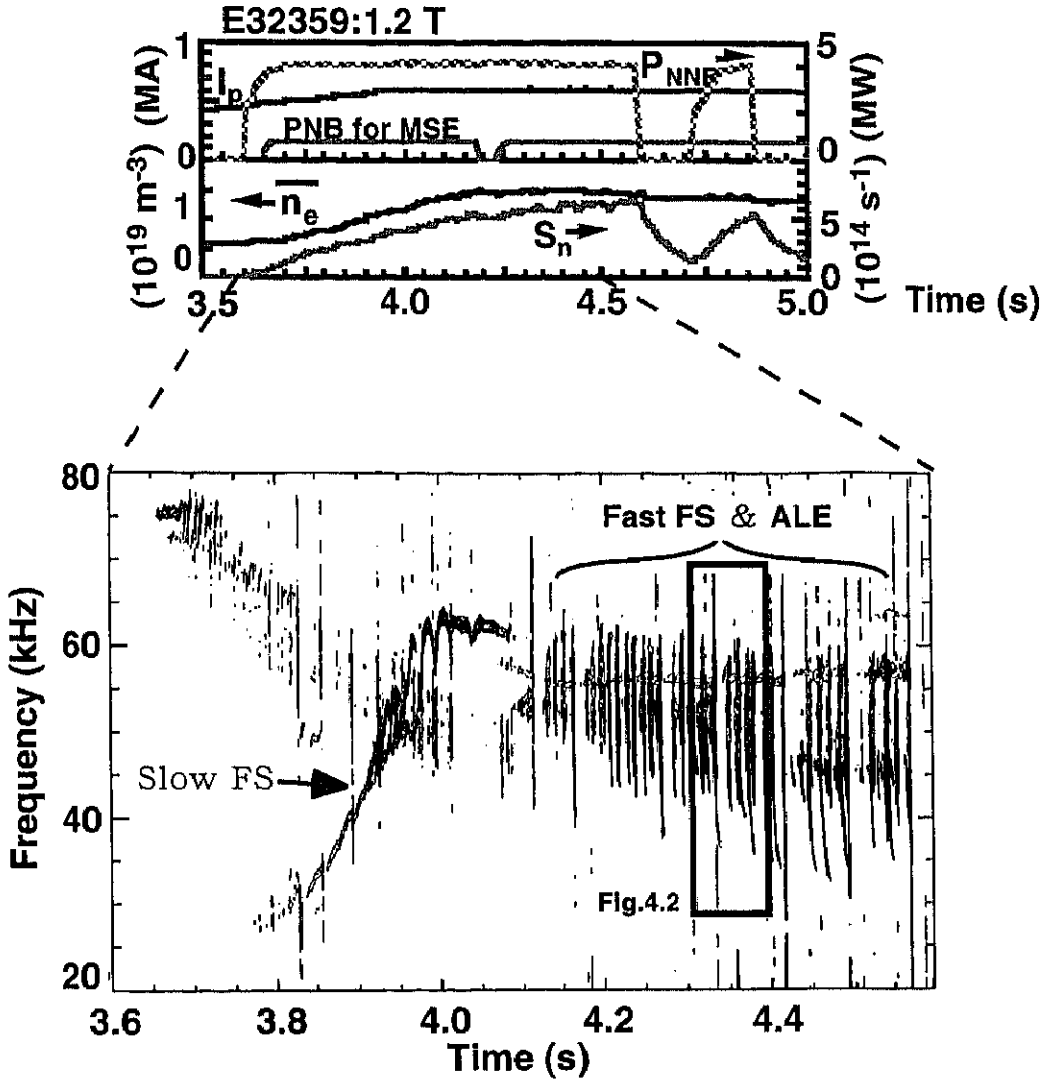

Figure 4.1 *Time trace of frequency spectrum of magnetic fluctuation measured by Mirnov coils at the first wall on a midplane in E32359.*

to develop with a frequency around 60 kHz and chirping by 10-20 kHz in 1-5m. These instabilities are burst-type modes. These modes were observed in/near the birth domain of ITER alpha particles in Fig.1.1.

4.1.2 Instability with slow frequency sweeping

The modes with large frequency sweeping appear at 0.15 to 0.2 s after the N-NB

injection as shown in Fig.4.1. The frequency started at about 30 kHz, which is below TAE frequency. The frequency sweeps up and reached maximum frequency at 65 kHz during 0.2 s. The saturation frequency is in range of TAE frequency. At the same time, another modes whose frequency sweeps down from upper range of TAE frequency were also observed. So far these modes with large sweeping frequency can't explain by the change of v_A or in frequency of TAE type modes.

4.1.3 Burst modes in the range of TAE frequency

After frequency saturated, bursting modes in the range of TAE frequency started. These modes is called "Fast frequency sweeping (FS) mode". Fast FS modes consist of bifurcating branches with the same start frequency which lies in TAE gap. Each branch changes its frequency by 10-20 kHz in 1-5 ms. These modes continue to be excited intermittently for several hundred milliseconds Fast FS modes can't be explained by the equilibrium parameter variation. Also another type of bursting modes with abrupt large amplitude was observed. Figure 4.2 shows the time trace of magnetic fluctuation amplitude in the frequency range of 30-70 kHz for 4.32 s < t < 4.37 s in Fig.4.1. These amplitude spikes in the magnetic fluctuation called "abrupt large-amplitude events (ALEs)". The ALEs have a time scale of 200 – 400 μs and the amplitude of ALEs reach $\tilde{B}_\theta / B_\theta \sim 10^{-3}$ at the first wall and are 5-100 times as large as that of Slow Fast FS modes. ALEs usually appear during the occurrence of Fast FS modes and have a peak amplitude at frequency similar to Fast FS modes.

4.1.4 Reversed–shear-induced Alfvén eigenmode (RSAE)

In reversed shear (RS) plasmas in JT-60U, AEs driven by energetic particles induced by ion cyclotron range of frequency (ICRF) heating were observed. These AEs have large and rapid upward chirping in the range of AE frequency as shown in Fig.4.3(a). These modes can not be explained by the change of TAE frequency, so far.

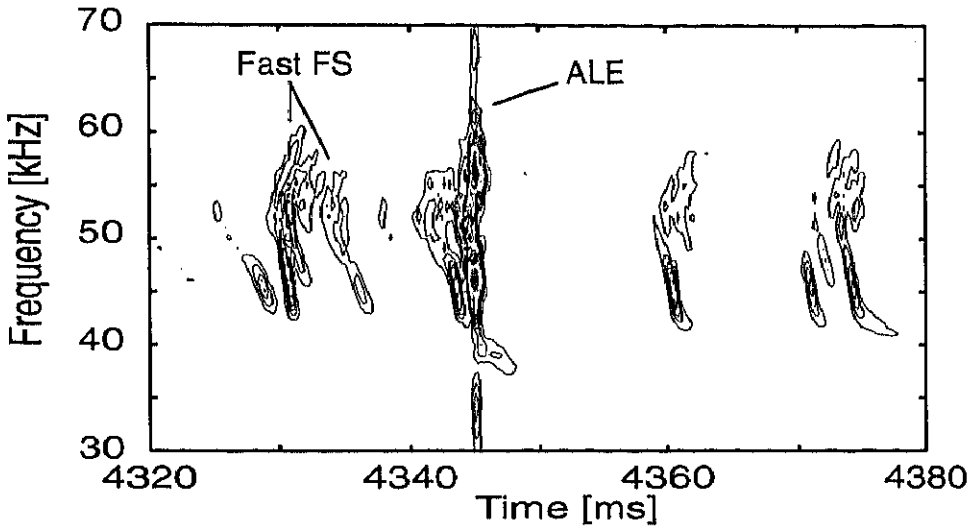

Figure 4.2 *Time trace of spectrum magnetic probe duringsome Fast FS modes and a ALE. for 4.32 < t <4.38 s and 30 < f < 70 kHz, which correspondign to the region enclosedby open square in figure 4.1*

However, a new theory of Reversed-Shear-induced Alfvén Eigenmode (RSAE) model was provided to interpret the observed fast and large frequency sweeping modes [7]. RSAE is a global AE near the zero shear region of the RS plasmas, and RSAE model further indicates transition from RSAE to TAE as q_{min} decrease. In order to confirm RSAE model AE experiments with high 3.73T toroidal field for the accurate reconstruction of q-profile were performed in N-NB injected hydrogen plasma. The results of these experiments demonstrate RSAE model can explain the large and rapid frequency sweeping in N-NB heated plasmas, and those subsequent saturation in the range of TAE frequency. Furthermore, RSAE model can also explain large and rapid upward frequency chirping observed in a ICRF heated RS plasma as shown Fig. 4.3(b). Furthermore, Slow FS mode, describing in Sec.4.1.2, can be interpreted by RSAE.

4.1.5 Enhanced transport of energetic ions

The drop of the neutron emission rate on the occurrence of ALEs and Fast FS modes with large amplitude of magnetic fluctuation was observed. Figure 4.4 shows time traces of frequency spectrum of magnetic fluctuations, the volume integrated neutron emission

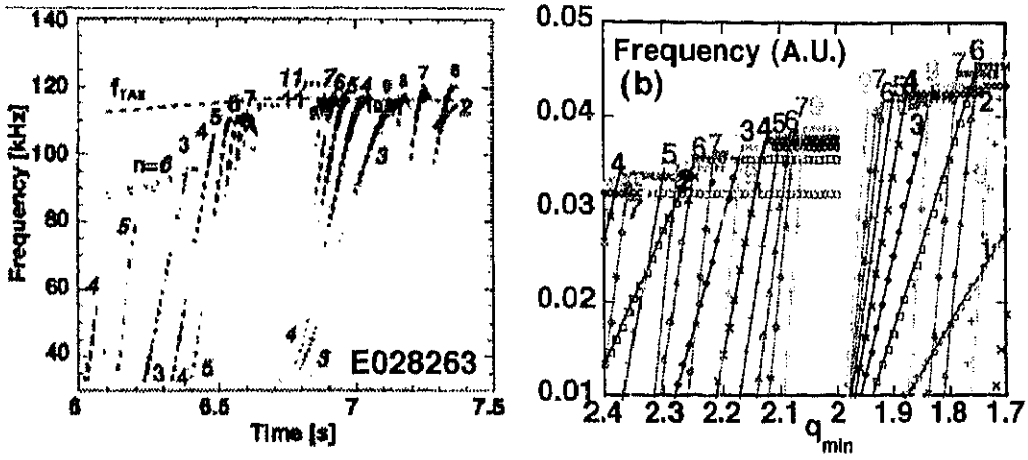

Figure 4.3 *(a) Typical temporal evolution of AE frequency changes observed in a JT-60U ICRF heated RS plasma. (b) The frequencies of n =1-9 RSAEs (solid sloping line) and TAEs (horizontal aligned marks) as a funtion of the* q_{min} *decrement.*

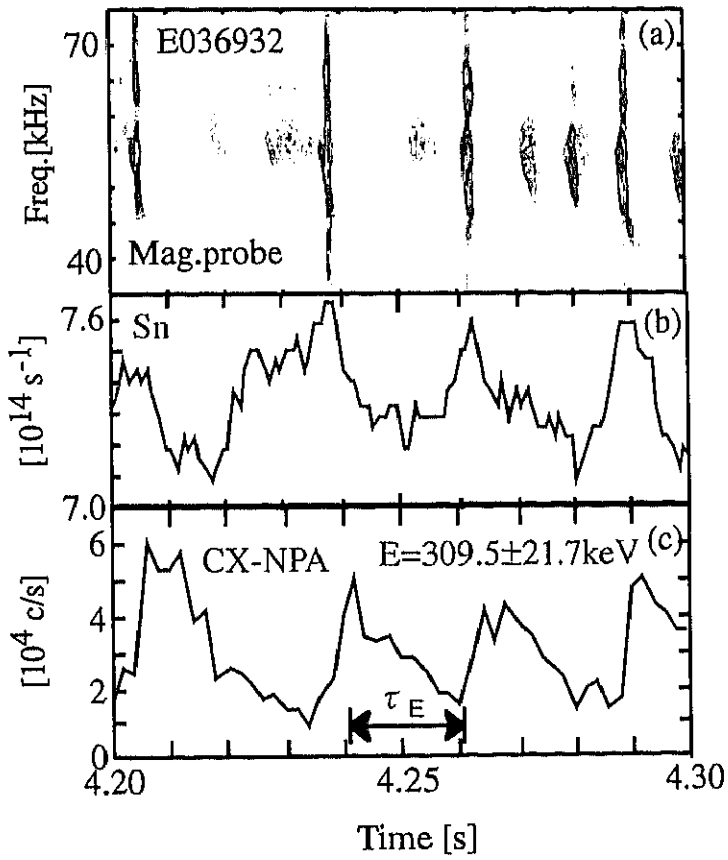

Figure 4.4 *(a)The time trace of magnetic fluctuations, (b) total neutron emission rate, and (c) neutral particle fluxes with energy of 309.5 ±21.7 keV measured by CX-NPA .*

rate, and the neutral particle fluxes with the energy of about 310 keV measured by charge exchange neutral particle analyzer (CX-NPA)[8]. When ALE occurs, significant drop of a volume integrated neutron emission rate, S_n, and enhanced fast neutral fluxes are observed. This result means ALEs cause an enhanced transport of energetic ions. Fast FS modes also cause an enhanced transport when its amplitude is large.

4.1.6 Application of neutron emission profile measurement to AE experiment using N-NB

As described above, drop of volume-averaged neutron emission rate by bursting modes was observed. This suggests that transport of energetic ion due to bursting mode such as ALEs is enhanced by N-NB. Study of energetic ion transport by ALEs is very important for the assessment of the transport of alpha-particles by AEs in ITER. It is not, however, clearly understood yet whether this transport is due to loss or redistribution of energetic ions, or both processes are important, since obtained neutron value was volume-averaged one. As mentioned in Chapter 3, we have established neutron emission profile measurement in JT-60U [9]. Since beam-thermal neutrons are dominant in such experiments with N-NB in JT-60U, change of the neutron emission profile indicates movement of energetic ions produced by N-NB. This makes the neutron emission profile measurement a useful for the study of transport of energetic ions. In this study, neutron emission profile measurement was applied to the AE experiment using NNB injection to investigate fast ion behavior for the first time.

In section 4.2, a basic theory of TAEs concerned in this study is described. Then, in section 4.3 we refer to the TAE experiments using N-NB, to which we applied neutron emission profile measurement, and its result. In section 4.4 we make a discussion for this experiment.

4.2 Basic theory of Alfvén eigenmode

In this section, the outline of basic theory of Toroidiricity-induced Alfvén Eigenmode, which is directly concerned our study.

4.2.1 Alfvén wave in uniform plasma

Alfvén waves in uniform plasma can be described by using ideal MHD equations and Maxwell's curl equations

$$\rho \frac{\partial \mathbf{v}}{\partial t} = \mathbf{j} \times \mathbf{B}_0 \qquad \mathbf{E} + \mathbf{v} \times \mathbf{B}_0 = 0 \tag{4.1}$$

$$\nabla \times \mathbf{b} = \mu_0 \mathbf{j} \qquad \nabla \times \mathbf{E} = -\frac{\partial \mathbf{b}}{\partial t} \tag{4.2}$$

where ρ is the plasma density, $\mathbf{B}_0$ is the steady magnetic field, and the quantities **v**, **j**, **E** and **b** are time varying quantities involved in wave propagation. Both ρ and $\mathbf{B}_0$ may vary with position but we assume in this section that they don't.

Eq.(4.1) and (4.2) can be solves either in Cartesian (x, y, z) or cylindrical (r, θ, φ) coordinates. Solutions for a cylindrical plasma will be examined in next section, 4.2.2. In this section we examine plane wave solutions of the form

$$e^{i(k_x x + k_y y + k_z z - \omega t)} \tag{4.3}$$

so that $\partial / \partial x = ik_x$, $\partial / \partial y = ik_y$, $\partial / \partial z = ik_z$ and $\partial / \partial t = -i\omega$. It is even simper to rotate the coordinate system so that k lies in the x-z plane (k_y=0) but we consider the case $k_y \neq 0$ for generality. Assuming that $\mathbf{B}_0$ is in the z direction, the components of equation (4.1) are

$$\left.\begin{array}{ll} -i\omega\rho v_x = j_y B_0 & E_x = -v_y B_0 \\ i\omega\rho v_y = j_x B_0 & E_y = v_x B_0 \\ v_z = 0 & E_z = 0 \end{array}\right\} \tag{4.4}$$

$$\therefore \quad i\omega\mu_0 j_x = \omega^2 E_x / v_A^2 \qquad i\omega\mu_0 j_y = \omega^2 E_y / v_A^2 \tag{4.5}$$

where $v_A^2 = B^2 / (\mu_0 \rho)$. Since E_z=0, the components of (4.2) are

$$\left.\begin{aligned} \mu_0 j_x &= i(k_y b_z - k_z b_y) \qquad \omega b_x = -k_z E_y \\ \mu_0 j_y &= i(k_z b_x - k_x b_z) \qquad \omega b_y = -k_z E_x \\ \mu_0 j_z &= i(k_x b_y - k_y b_x) \qquad \omega b_z = k_x E_y - k_y E_x \end{aligned}\right\} \tag{4.6}$$

From equations (4.5) and (4.6),

$$\left.\begin{aligned} (k_y^2 + k_z^2 - \omega^2 / v_A^2) E_x &= k_x k_y E_y \\ (k_x^2 + k_z^2 - \omega^2 / v_A^2) E_y &= k_x k_y E_x \end{aligned}\right\} \tag{4.7}$$

$$\therefore \quad (k_y^2 + k_z^2 - \omega^2 / v_A^2)(k_x^2 + k_z^2 - \omega^2 / v_A^2) = k_x^2 k_y^2 \qquad \text{or}$$

$$(\omega^2 / v_A^2 - k_{//}^2)(\omega^2 / v_A^2 - k^2) = 0 \tag{4.8}$$

where $k_{//} = k_z$, $k_\perp^2 = k_x^2 + k_y^2$ and $k^2 = k_{//}^2 + k_\perp^2$.

The two solutions of Eq.(4.8) are

$$\omega / k_{//} = v_A \quad \text{Shear wave} \tag{4.9}$$

$$\text{and} \quad \omega / k = v_A \quad \text{Compressional wave} \tag{4.10}$$

Using these solutions, we can find the electric field components from Eq.(4.7), the magnetic field components from Eq.(4.6), and the v components from Eq.(4.4), as follows:

SHEAR	COMPRESSIONAL
$E_y / E_x = k_y / k_x$	$E_y / E_x = -k_y / k_x$
$E_z = 0$	$E_z = 0$
$b_y / b_x = -k_x / k_y$	$b_y / b_x = k_y / k_x$
$b_z = 0$	$b_z / b_y = -k_\perp / (k_y k_{//})$
$\nabla \cdot \mathbf{E} = i\mathbf{k} \cdot \mathbf{E} \neq 0$	$\nabla \cdot \mathbf{E} = 0$
$\nabla \cdot \mathbf{v} = i\mathbf{k} \cdot \mathbf{v} = 0$	$\nabla \cdot \mathbf{v} = i\omega b_z / B$
$\nabla \cdot \mathbf{b} = i\mathbf{k} \cdot \mathbf{b} = 0$	$\nabla \cdot \mathbf{b} = i\mathbf{k} \cdot \mathbf{b} = 0$

The phase velocity of the shear wave in a direction parallel to $\mathbf{B_0}$ is equal to v_A, regardless of the direction of $\mathbf{k}$. The phase velocity of the compressional wave is equal to v_A, regardless of the direction of $\mathbf{k}$. If θ is the angle between $\mathbf{k}$ and $\mathbf{B_0}$, then $\omega / k = v_A \cos\theta$ for the shear wave and $\omega / k = v_A$ for compressional wave.

The shear wave is partly electrostatic, resulting in charge separation. Purely electrostatic waves have $\mathbf{E}$ parallel to $\mathbf{k}$, so $\nabla \times \mathbf{E} = i\mathbf{k} \times \mathbf{E} = i\omega\mathbf{b} = 0$. The shear wave does not involve any compression of the plasma since $\nabla \cdot \mathbf{v} = 0$. The compressional

wave, as its name implies, acts to compress the plasma but there is no charge separation.

4.2.2 Shear Alfvén waves in non-uniform cylindrical plasma

In this section, we mention for only Shear Alfvén waves, which directly concern with TAE. In a cylindrical plasma with cylindrical (r, θ, φ) coordinates, setting a wave number and magnetic on $\mathbf{k} = (k_r, k_\theta, k_\varphi)$ and $\mathbf{B} = (0, B_\theta, B_\varphi)$ on 'magnetic surface' with r = constant,

$$\mathbf{k} \cdot \mathbf{B} = k_\theta B_\theta + k_\varphi B_\varphi = k_{//} B. \tag{4.11}$$

Assuming that plasma length of a vertical direction (φ direction) is $2\pi R_0$ taking into account for the expansion to toroidal plasma, and that the poloidal mode number and toroidal mode number are m and n, respectively, furthermore that perturbation is represented quantities by form $e^{i(m\theta - n\varphi - \omega t)}$, since $k_\theta = m/r$ and $k_\varphi = -n/R$, a wave number parallel to magnetic field is given by

$$k_{//} = \frac{k_\theta B_\theta + k_\varphi B_\varphi}{B}$$

$$= \frac{1}{R}\left(\frac{m}{q} - n\right). \tag{4.12}$$

Therefore, the dispersion equation in Eq.(4.9) is given by

$$\omega^2 = \frac{1}{R_0^2}\left(\frac{m}{q} - n\right)^2 V_A^2. \tag{4.13}$$

For each (m, n) the frequency ω is given by Eq.(4.13). Various investigations of shear Alfvén waves in cylindrical plasmas have also indicated existence of discrete stable global Alfvén eigenmodes with below the minimum of the Alfvén continuum for given (m, n). They are called "cylindrical global Alfvén waves". Figure 4.5 shows the profiles of shear Alfvén spectrum for poloidal mode number of 1, 2 and 3 on toroidal mode number of 1 in the non-uniform cylindrical plasma which has following parameter: plasma density profile, $n_i = n_0(1 - 0.1\rho^2)$ and $q = 1 + \rho^2$, where $\rho(= r/a)$ is the normalized minor radius, and n_0 is the central ($\rho = 0$) density. As shown in Fig.4.5, since

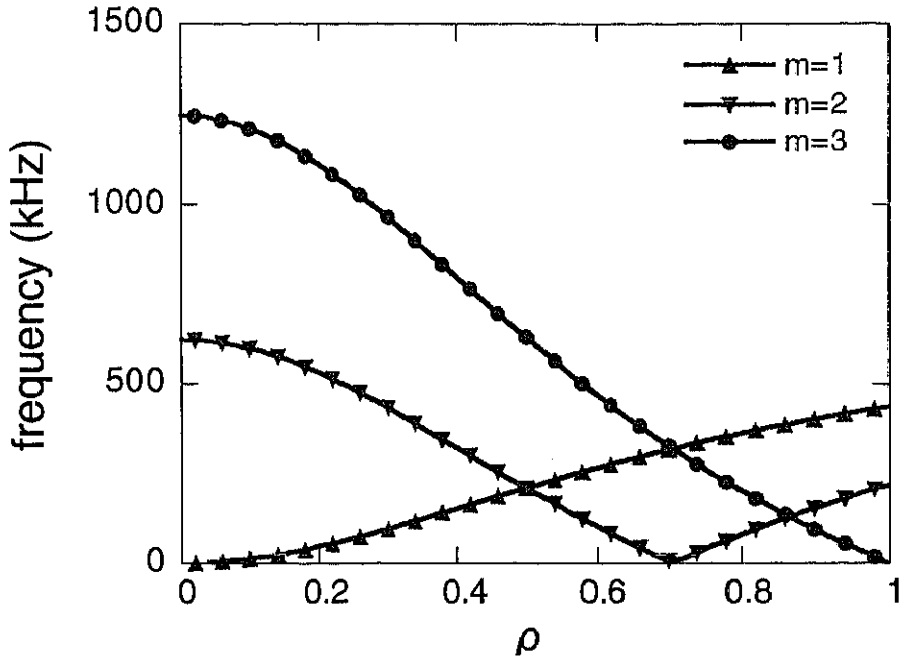

Figure 4.5 *Shear Alfvén spectrum in in the non-uniform cylindrical plasma which has following parameter: plasma density profile,* $n_i=n_o(1-0.1\,\rho)$ *and* $q=1+2\,\rho^2$

the spectrum is continuum function, this is called 'continuum spectrum'.

4.2.3 Toroidricity-induced Alfvén eigenmodes

In toroidal geometry there is an interaction between among the neighboring poloidal harmonics and it can break up the shear Alfvén continuous with gaps [10].

For ideal MHD equation:

$$\mathbf{J}\times\mathbf{B}=\nabla p, \quad \nabla\times\mathbf{B}=\mathbf{J}, \quad \text{and} \quad \nabla\cdot\mathbf{B}=0, \tag{4.14}$$

we employ plasma displacement ξ with time dependence

$$\xi(\mathbf{x},t)=\xi(\mathbf{x})e^{-i\omega t}, \tag{4.15}$$

where J, B and p are the equilibrium current, magnetic field, and plasma pressure, respectively.

Introducing the Fourier expansion of perturbation for calculation of perturbation quantities, then variational calculation is equivalent to the determination of eigenvalues

and eigenfunctions.

Employing a large aspect ratio, low-β equilibrium by Greene et al. [11], the flux surfaces of symmetric equilibrium can be expressed by

$$\begin{aligned} X &= R - \varepsilon r\cos\theta - \varepsilon^2\Delta(r) + \varepsilon^3[E(r)+G(r)]\cos\theta + \cdots \\ Z &= \varepsilon r\sin\theta + \varepsilon^3[E(r)-G(r)]\sin\theta + \cdots \end{aligned} \tag{4.15}$$

where ε is tag denoting the order of the perturbation expansion, r labels the flux surface and $\Delta(r)$ measures the shift of the center of the surfaces from the magnetic axis, E(r) determines the ellipticity of the surface, and G(r) modifies the labeling of the surfaces. Using Eq.(4.15), for each Fourier mode of perturbation the perturbation equation

$$\begin{aligned} &\frac{2\pi\varepsilon^2 G(r)}{\alpha(r)B_0^2}\sum_{m,m'}\Big\{\Omega^2[\delta_{m,m'}+\varepsilon(\frac{r}{R}+\Delta'+\sigma)(\delta_{m,m'-1}+\delta_{m,m'+1})] \\ &(m-nq)(m'-nq)[\delta_{m,m'}+\varepsilon(\frac{r}{R}+\Delta'-\sigma)(\delta_{m,m'-1}+\delta_{m,m'+1})]+O(\varepsilon^2)\Big\}a_m a_{m'}^* = 0 \end{aligned} \tag{4.16}$$

is given, where $\Delta' = d\Delta(r)/dr$, $\Omega^2 = \omega^2\rho\alpha^2(r)$, $\delta_{m,m'}$ is the Kronecker delta. To $O(\varepsilon)$ only couplings of neighboring poloidal harmonics are present. Couplings of poloidal harmonics with m differing more than one come in $O(\varepsilon^2)$ term, which are neglected in Eq.(4.16). Now keeping only m and m+1 modes, we have dispersion relation

$$\begin{vmatrix} (\Omega^2-\Omega_0^2) & \varepsilon[(r/R+\Delta'+\sigma)\Omega^2-(r/R+\Delta'-\sigma)\Omega_0\Omega_1] \\ \varepsilon[(r/R+\Delta'+\sigma)\Omega^2-(r/R+\Delta'-\sigma)\Omega_0\Omega_1] & (\Omega^2-\Omega_1^2) \end{vmatrix} = 0, \tag{4.17}$$

where $\Omega_0 = (m-nq)$, $\Omega_1 = (m+1-nq)$. Near the crossing surfaces of Ω_0^2 and Ω_1^2 where $|\Omega_0^2-\Omega_1^2| \le 0(\varepsilon^2)$, we have $\Omega_0 \cong -\Omega_1$ and $\Omega_0^2 \approx (1/4)$. Then the eigenvalue Ω^2 is approximately given by

$$\Omega_\pm^2 = \Omega_0^2[1 \pm 2\varepsilon(r/R+\Delta') + O(\varepsilon^2)]. \tag{4.18}$$

Figure 4.6 gives the graph of Ω for n=1 and m=1 calculated from Eq.(4.18), where the eigenvalues are plotted versus the normalized minor radius $\rho = r/a$. The normalization frequency is also defined for the eigenvalues. The broken curves represent the continuous spectra for Ω_0^2 and Ω_1^2 in absence of toroidal couplings and the solid curves represent Ω calculated from Eq.(4.18). although he former cross, in the case of the latter there is the gap near the frequency at crossing Ω_0^2 and Ω_1^2 due to toroidal coupling by the effect

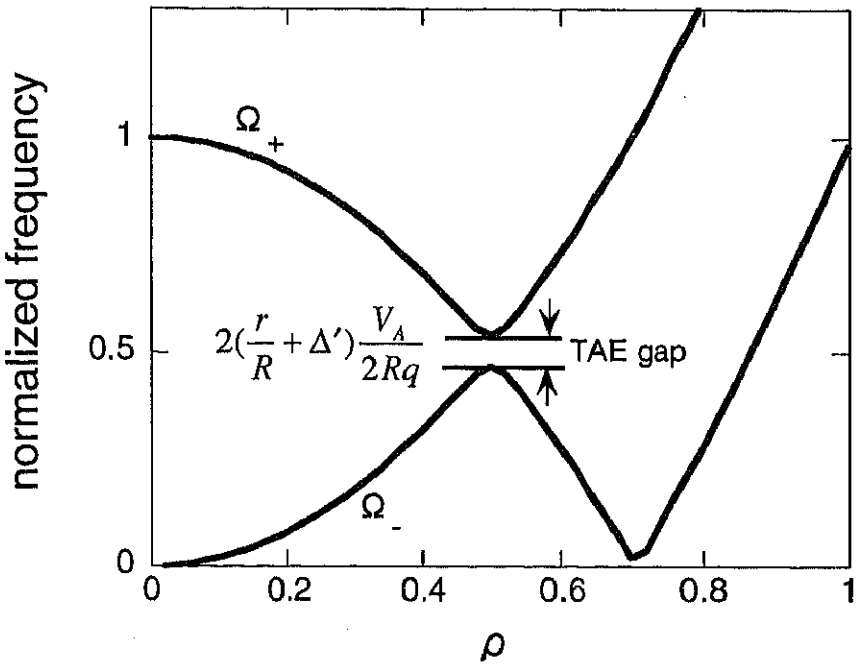

Figure 4.6 *Shear Alfvén spectrum in toroidal plasma. There is gap near the frequency at crossing* Ω^+ *and* Ω^- *due to toroidal coupling by there effect of toroidal geometry.*

of toroidal geometry. This is called " TAE gap". The wide of the gap $|\Omega_+ - \Omega_-|$ is about $2(\frac{r}{R}+\Delta')\frac{V_A}{2Rq}$.

4.2.4 Excitation of toroidricity-induced Alfvén eigenmode and damping mechanism by fast ions

The stability of TAEs depends on the fast ion (alpha particle) pressure gradient and several dissipative mechanisms. Calculation of driving and damping leads to a growth rate γ given by

$$\frac{\gamma}{\omega_0} \approx \frac{9}{4} + \beta_\alpha \left(\frac{\omega_{*\alpha}}{\omega_0} - \frac{1}{2} \right) F\left(\frac{V_A}{V_\alpha} \right) \text{-D}, \tag{4.19}$$

where

$$\omega_0 = \frac{V_A}{2qr}$$

is the real frequency of basic Alfvén mode, with V_A is the Alfvén velocity, β_α is the beta value of the α-particles and $\omega_{*\alpha}$ is their diamagnetic frequency, given for poloidal mode number m by

$$\omega_{*\alpha} = -\frac{m}{r}\frac{T_\alpha}{e_\alpha B}\frac{d\ln n_\alpha}{dr}.$$

V_α is the average α-particle velocity and $F(x) = x(1+2x^2+2x^4)e^{-x^2}$. The second term in the right hand side of Eq.(4.19) is a excitation term of instabilities by α-particles, the last term, D is damping term by several damping mechanisms. Eq.(4.19) shows that the more β_α is high and also $\omega_{*\alpha}$ is large, which mean α-particle is localized spatially, further poloidal mode number m is large , the more TAEs become to unstable. In the damping term, there are continuum damping [12-15] and radiative damping [16], ion Landau damping [17], electron Landau damping [18], and trapped electron collisional damping [19, 20] and so on.

Various numerical codes were developed to interpret the Alfvén eigenmodes observed in fast ion experiments on present day large tokamaks. For the NOVA-K kinetic MHD hybrid stability code [21, 22] was used extensively to analyze TFTR stability and also applied to study in JT-60U with high energy (0.5MeV) NNBI [23] as well as with ion cyclotron resonant heating [24]. In general, the theoretical frequency and mode structure have been found to match the experimental measurements quite well, while the stability thresholds more difficult to calculate, are in reasonable agreement.

4.3 AE experiment using N-NB [25]

4.3.1 Experimental condition

We performed AE experiment using N-NB injection in the plasma with following parameter: I_p=0.6MA, B_T=1.2T, P_{NNB}=5MW, E_{NNB}>390keV, where P_{NNB}, E_{NNB} are power and energy of N-NB, respectively. P-NB was also injected for diagnostics of ion temperature and q-profile.

In Alfvén eigenmode (AE) experiment, it is necessary that the beam ion velocity

parallel to the magnetic field, $v_{b//}$, is to be comparable to the Alfvén velocity, v_A ($= B / \sqrt{\mu_0 \rho}$). In this reason, these experiments were carried out in the low magnetic field of B_T=1.2T.

Figure.4.7 shows the plasma configuration and sight lines of Neutron emission profile measurement at t=4.5s. The sight line of the innermost channel passes through r/a ~ 0.21 while that of the outermost channel is at r/a ~ 0.86.

The ratio of the beam ion velocity parallel to the magnetic field to the Alfvén velocity, $v_{b//}/v_A = 1.08$, and the volume averaged hot ion beta, $<\beta_h>$ was about 0.6% in this discharge. The parameter domain of fast ions in this discharge is marked in Fig.1.1. This parameter domain for fast ions produced by N-NB injection in this experiment is near the birth domain of particles in ITER.

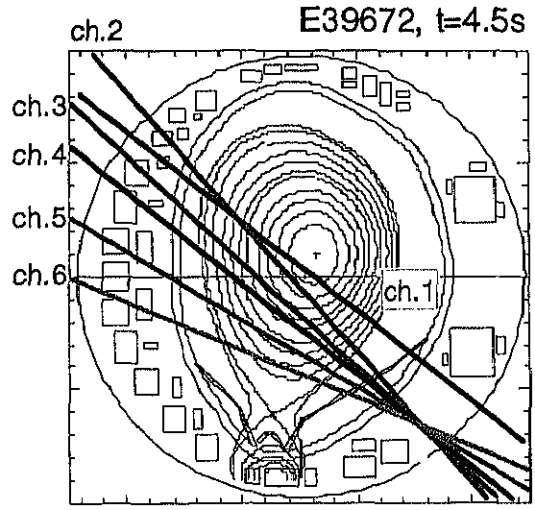

Figure 4.7 *Plasma configuration and the sighit line of neutron emission profile measurement at 4.5s in E39672*

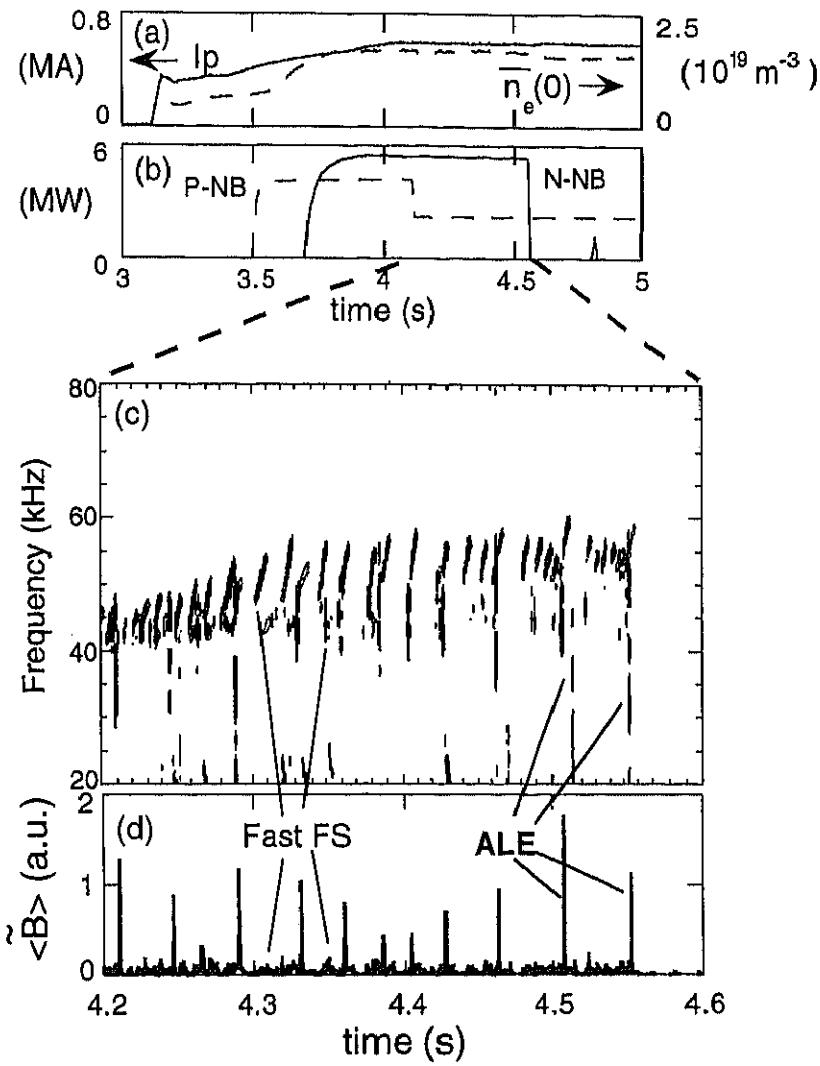

Figure 4.8 *Time trace of typical plasma parameters of E39672. (a): plasma current, I_P and Central electron density ($n_e(0)$). (b): input power of N-NB and P-NB. The beam energy of N-NB is 397keV. (c): Frequency spectrum of magnetic fluctuations measured by Mirnov coil located near the first wall at the outer midplane. (d) mode amplitude of magnetic fluctuations.*

4.3.2 Observation the bursting mode in the range of TAE gap frequency

Figure 4.8 shows the waveforms of plasma parameters. Figure. 4.8(a) shows the time trace of plasma current and line-averaged electron density. Figure. 4.8(b) shows the time trace of the input power of N-NB and P-NB. Figure. 4.8(c) shows the time trace of the frequency spectrum of a magnetic probe signal measured by a Mirnov coil located

near the first wall. At t = 4.5 s $n_e(0) \sim 2.3 \times 10^{19} m^{-3}$, $T_e(0) \sim 1.6$keV, $T_i(0) \sim 1.4$keV, and $Z_{eff} \sim 2.0$, where $n_e(0)$, $T_e(0)$ and $T_i(0)$ are electron density, electron temperature and ion temperature at the plasma center, respectively, and Z_{eff} is the effective charge. T_i is measured by the charge exchange recombination spectroscopy [26]. n_e and T_e are measured by the Thomson scattering [27].

Two kinds of bursting modes were observed during N-NB injection as shown in Fig. 4.8(c). One is Fast FS mode. The other is ALE. The properties of these modes were described in Sec.4.1.3

4.3.3 The change of neutron emission rate by bursting modes.

The time trace of the neutron emission rate during N-NB injection is shown in Fig. 4.9 together with the magnetic fluctuation amplitude. Figure 4.9(a) shows the time trace of the total neutron emission rate measured by the fission chamber [28]. Figure 4.9(b) shows the time trace of the neutron emission rate of each channel measured by the neutron emission profile monitor, with the innermost channel at the top. The magnetic fluctuation amplitude in the frequency range of 20~80kHz is shown in Fig. 4.9(c). When ALEs occurred, the neutron emission rate was significantly changed. The total neutron emission rate is reduced during the occurrence of ALEs as shown in Fig. 4.9(a). At t = 4.51s, the total neutron emission is reduced by 7.8%. The neutron emission signals from the central region ($r/a < 0.20$) reduced, while signals from the peripheral region ($r/a > 0.48$) increased. However, because the relative change of several channels was not large, we also performed an ensemble average of the change of each channel over all ALEs during N-NB injection. The change of each channel is shown in Fig. 4.10. One can see that the neutron emission rate in the central region decreased, while that in the peripheral region increased. Since neutrons produced via beam-thermal reaction account for over 90% of the total neutron emission in the N-NB experiments according to the calculation by TOPICS code [29] and by taking into account the absence of change in ion

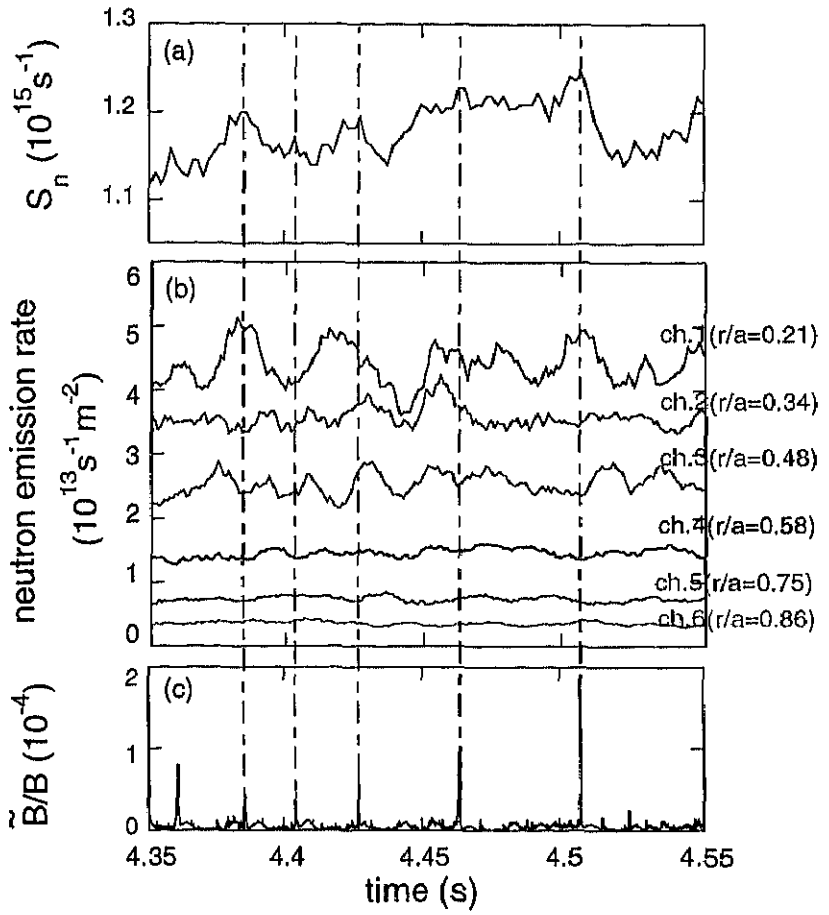

Figure 4.9 *Neutron signals during the occurrence of ALEs. (a): Total neutron emission measured by Fission chamber, (b) the signals of the neutron emission profile monitor. The innermost channel is shown on top. And (c): mode amplitude of magnetic fluctuations.*

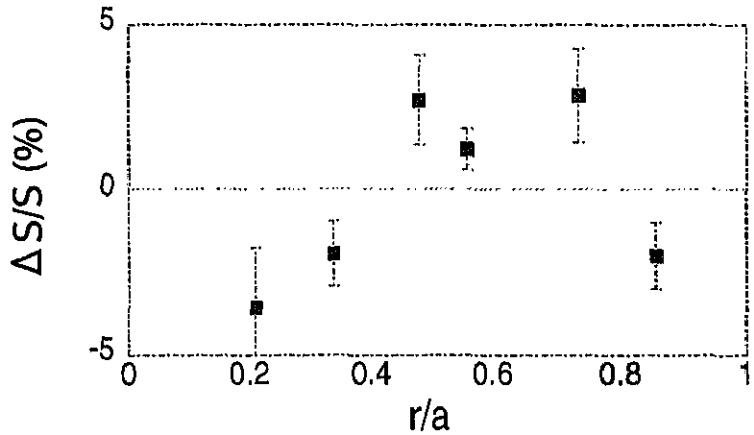

Figure 4.10 *Change rate of the signals of neutron emission profile measurement due to ALEs.*

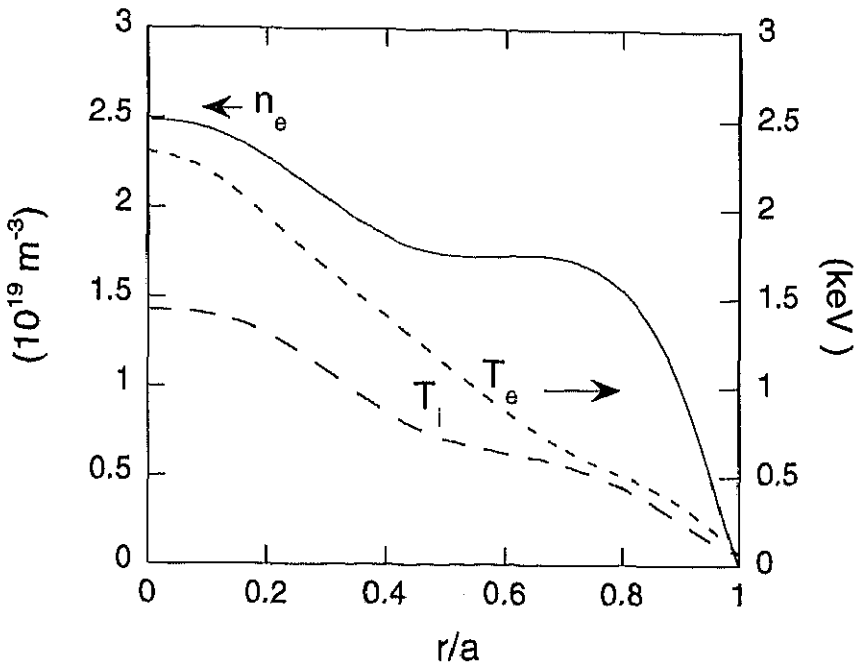

Figure 4.11 *Profiles of electron density, temperature and ion temperature at t = 4.51 s*

temperature and electron density, the observed change of the neutron emission profile must be attributed to the transport of fast ions.

To understand the fast ion transport caused by ALEs we choose a representative time slice at t = 4.51 s. Figure 4.11 shows the profiles of electron density and ion temperature. The neutron emission rate of all channels before and after the ALE, which occurred at t = 4.51 s, is presented in Fig. 4.12. One can see that the profile has broadened. However, because the line-integrated neutron emission rate along each sight line are shown in Fig.4.12, we have to employ the Abel inversion method to obtain the neutron emission density profile. We used the Abel inversion by Wiener Filter method in JT-60U [30]. In this Abel inversion, it was assumed so that the value at r/a = 1 may become to 0. Since the Abel inversion with Wiener Filter method defines a spatial profile from the outer region and the sight line of the innermost channel passed through at r/a ~ 0.21 in this discharge, the profile of the center region without the sight line was uncertain, and the possibility of a peak in the very center could not be ruled out. The total neutron

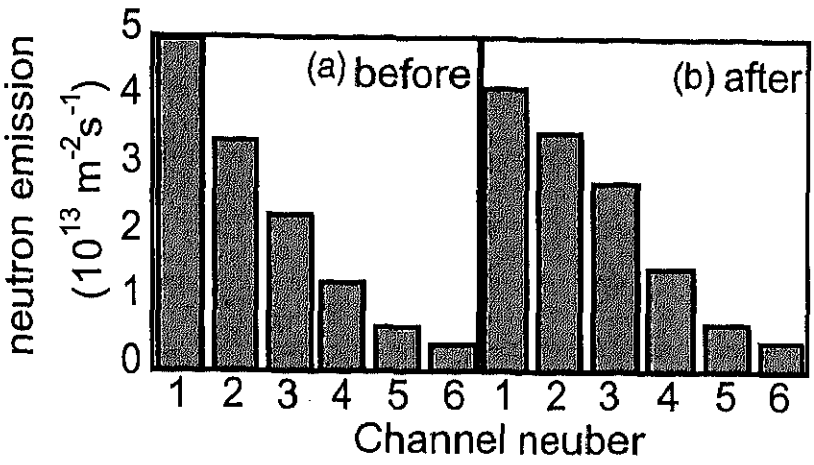

Figure 4.12 *Line-integrated neutron emission profile before, (a), and after, (b), the ALE at t = 4.51 s*

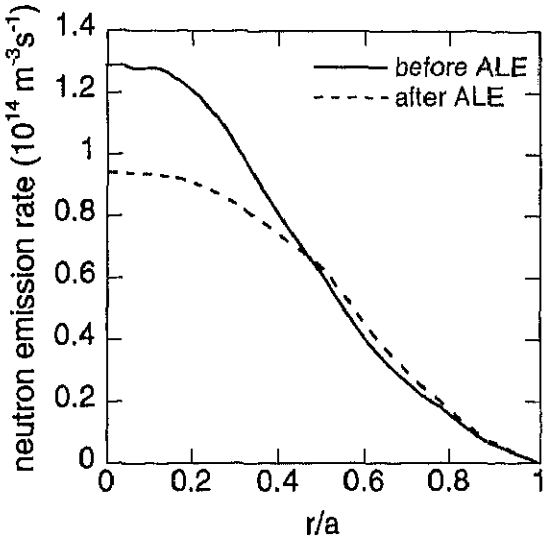

Figure 4.13 *Neutron emission profile obtained by Abel inversion before and after ALE at t = 4.51 s*

emission rate estimated by integrating Abel inverted neutron emission density profile was found to be smaller than the measured total neutron emission rate. For this reason, the neutron emission density profile in the region of r/a < 0.21 was decided in order to be made to agree with the measured total neutron emission rate. The neutron emission

density profile obtained by such a procedure is shown in Fig.4.13.

4.3.4 Estimation of transport of fast ion by bursting modes

To estimate the transport of fast ions from the neutron profile change, we assume for simplicity that the fusion reaction is only due to beam-thermal reaction. In the calculation using the TOPICS code, it has been estimated that the beam-target ion reaction accounts for over 90 % of the total neutron emission rate in such an experiment with N-NB. Therefore, the fusion reactivity

$$\langle \sigma v \rangle = \iint dv_1 dv_2 f(v_1) f(v_2) \sigma(v') v' \qquad v' = v_1 - v_2$$

can be well approximated by the beam-target reactivity. The beam-target reactivity for a mono-energetic beam of speed v_b reacting with Maxwellian target ions with thermal speed v_{th} [31] is shown in Eq.(3.11):

$$\langle \sigma v \rangle_{bt} = \frac{1}{v_b v_{th} \sqrt{\pi}} \int \sigma v^2 \left[\exp\left(-\left(\frac{v - v_b}{v_{th}} \right)^2 \right) - \exp\left(-\left(\frac{v + v_b}{v_{th}} \right)^2 \right) \right] dv. \qquad (4.22)$$

The total reactivity is obtained by averaging $\langle \sigma v \rangle_{bt}$ over the beam energy distribution. For the fusion cross section σ in Eq. (4.22), we employ the equation presented by Bosh et al. [32],

$$\sigma(E) = \frac{S(E)}{E \exp(B_G / \sqrt{E})} \qquad (4.23)$$

where E denotes the energy in the center-of-mass frame, $B_G = \pi \alpha_c Z_{th} Z_b \sqrt{2 \mu_{red} c^2}$ is the Gamov constant for reacting particles with atomic number Z_{th} and Z_b, $\mu_{red} = m_{th} m_b / (m_{th} + m_b)$ is the reduced mass, α_c is the fine structure constant, and S(E) is the astrophysical S-function. Here, a Pade's polynomial as shown in Eq.(3.7) is employed for S(E) :

$$S(E) = \frac{A_1 + E\left(A_2 + E\left(A_3 + E\left(A_4 + EA_5\right)\right)\right)}{1 + E\left(B_1 + E\left(B_2 + E\left(B_3 + EB_4\right)\right)\right)}. \qquad (4.24)$$

Each value of coefficient in Eq.(4.24) is given in $D(D,n)^3He$ reaction in Table 3.1.

Therefore, the neutron emission rate S_n is given by

$$S_n = n_{th} n_b \cdot (\sigma v)_{bt}, \tag{4.25}$$

where n_{th} and n_b are the density of target plasma and beam ions, respectively, $(\sigma v)_{bt}$ is the averaged $\langle \sigma v \rangle_{bt}$ over the beam energy distribution. We also assume that the energy distribution function of beam ions obeys the Stix's stationary solution f_{STIX} [33], where $\int_0^{E_b} f_{STIX} = 1$ and E_b is the injected beam energy. S_n is obtained from Fig.4.13 and n_{th} is obtained from the measured data. $(\sigma v)_{bt}$ is estimated by the above calculation, so that we can obtain the fast ion density n_b. To obtain the n_b spatial profile, we divide the normalized minor radius into 51 sections and calculate n_b in each section. We then compare the n_b profiles before and after the occurrence of ALE.

Before the occurrence of ALE, the fast ion density profile can be calculated by Eq.(4.25). It was reported from Shinohara et al. [6] that fast neutral fluxes caused by bursting TAE modes such as ALEs satisfied the resonant condition between the modes and the energetic ions. The resonant condition can be expressed as $N = (f / f_c)q - nq + m$ [34], where N is an integer, f is the mode frequency, f_c is the beam ion toroidal transit frequency, n is the toroidal mode number, m is the poloidal mode number, and q is the safety factor. Thus, to obtain the beam ion density after the occurrence of ALE, we assume that only fast ions in an energy range satisfying the resonant condition are transported by ALEs. Moreover, we assume that the transported fast ion energy range is independent of the radial distance.

The fast ion density after the occurrence of ALE, n_{after}, is derived as follows. By setting the energy range which satisfies the resonant condition to be $[E_{reso.MIN}, E_{reso.MAX}]$ for the beam ions, the neutron emission rate due to fast ions before the occurrence of ALE n_{before} is given by Eq.(4.25) and can be expressed as

$$\begin{aligned} S_{before} &= n_{before} n_{th} (\sigma v)_{bt} \\ &= n_{before} n_{th} \left[\left\{ \langle \sigma v \rangle_{bt} \Big|_0^{E_{reso.MIN}} \right\} + \left\{ \langle \sigma v \rangle_{bt} \Big|_{E_{reso.MIN}}^{E_{reso.MAX}} \right\} + \left\{ \langle \sigma v \rangle_{bt} \Big|_{E_{reso.MAX}}^{E_b} \right\} \right], \end{aligned} \tag{4.26}$$

where $\langle \sigma v \rangle_{bt} \Big|_{E_1}^{E_2}$ means the average fusion reactivity over the energy region of E_1 to E_2,

while for after the occurrence of ALE, assuming that beam ion density in the range of $[E_{reso.MIN}, E_{reso.MAX}]$ changes by a factor of x compared with that of before the occurrence of ALE, the neutron emission rate of AFTER, S_{after}, is given by

$$S_{after} = n_{before} n_{th} \left[\left\{ \langle \sigma v \rangle_{bt} \Big|_{0i}^{E_{reso.MIN}} \right\} + \left\{ \langle \sigma v \rangle_{bt} \Big|_{E_{reso.MAX}}^{E_b} \right\} \right] + \left(x n_{before} \right) n_{th} \left[\left\{ \langle \sigma v \rangle_{bt} \Big|_{E_{reso.MIN}}^{E_{reso.MAX}} \right\} \right]. \quad (4.27)$$

Subtracting Eq.(4.25) from Eq.(4.26), x can be found from

$$S_{after} - S_{before} = (x-1) n_b n_{th} \left\{ \langle \sigma v \rangle_{bt} \Big|_{E_{reso.MIN}}^{E_{reso.MAX}} \right\}$$

$$\therefore x = 1 + \frac{S_{after} - S_{before}}{n_b n_{th} \left\{ \langle \sigma v \rangle_{bt} \Big|_{E_{reso.MIN}}^{E_{reso.MAX}} \right\}} \quad . \quad (4.28)$$

Therefore, n_{AFTER} is given by

$$n_{after} = n_{before} \left[\int_0^{E_{reso.MIN}} f_{STIX}(E) dE + \int_{E_{reso.MIN}}^{E_b} f_{STIX}(E) dE \right]$$

$$+ x \cdot n_{before} \left[\int_{E_{reso.MIN}}^{E_{reso.MAX}} f_{STIX}(E) dE \right] \quad , \quad (4.29)$$

where $f_{STIX}(E)$ is a normalized distribution function of the Stix's stationary solution as mentioned above.

Figure 4.14 shows the fast ion density profiles before and after the occurrence of ALE as estimated from Eq.(4.25) and (4.29), respectively. The total fast ion population integrated over the volume is reduced by 6 % by the ALE, with a 20 % reduction in the central region of r/a < 0.4. This estimate indicates that ALEs expel a significant fast ion population from the core to the outer region (radial redistribution), with a part of it being lost from the plasma to the wall.

4.3.5 Enhancement of neutral particle flux by ALE

An increase of high energy neutral particle flux was also observed during the occurrence of ALEs [4]. Figure. 4.3 shows the time trace of the magnetic fluctuation frequency spectrum, the total neutron emission rate, and the neutral particle flux with energy of about 309.5 ± 21.7keV for the discharge E36932 reported in Ref[6]. The neutral particle flux is measured by the charge exchange neutral particle analayzer (CX-

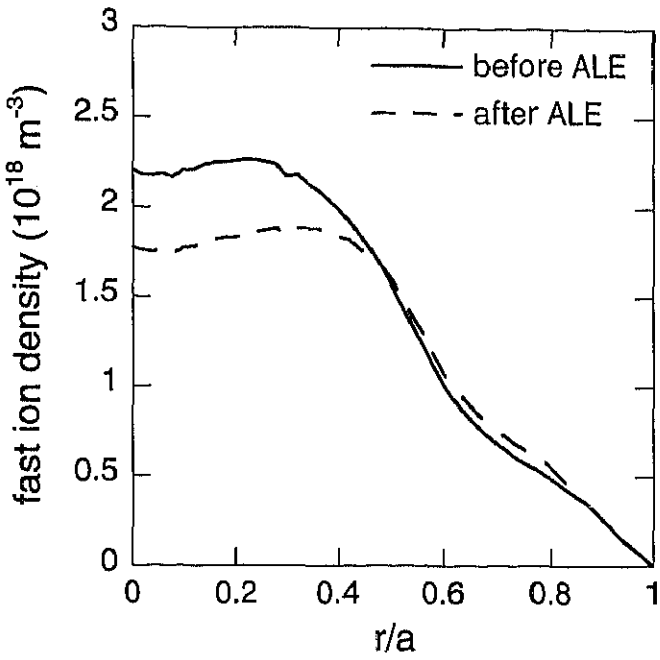

Figure 4.14 *Fast ion density profiles before and after ALE at t = 4.51 s.*

NPA) [8]. The plasma parameters of this discharge are I_p=0.6MA, B_T=1.2T, P_{NNB}=4MW, and E_{NNB}~360keV. As shown in Fig. 4.3, not only the decrease of the total neutron emission rate but also the increase of the neutral particle flux was observed during the occurrence of ALEs. Fast neutral fluxes are enhanced by the neutralization of fast ions caused by the interaction with neutral prticles in the peripheral region. The energy range of the enhanced neutral particle fluxes corresponds to the same energy range of the resonance condition [16]. The decay time in the energy window of 309.5±21.7 keV of CX-NPA, τ_E, is about 20ms as shown in Fig.4.3(c). If the energy decay of the fast ion flux is due to slowing down of energetic ions, then the decay time τ_d can be written as

$$\tau_d = \frac{\Delta E}{\langle dE/dt \rangle},$$

where ΔE is the width of the energy window of each channel of CX-NPA and is about

$\Delta E / E \sim 0.1 - 0.2$ here, and $\langle dE/dt \rangle$ is the change rate of fast ion energy and is given by

$$\left\langle \frac{dE}{dt} \right\rangle = -\frac{2}{\tau_s} E,$$

where τ_s is the slowing down time of fast ions. Since τ_s=0.2-0.3s at the peripheral region for this discharge, $\tau_d \approx 14 \sim 20$ms. Therefore $\tau_E \approx \tau_d$, and the decay time of the neutral particle fluxes can be explained by the slowing-down of fast ions. This suggests that the transport of energetic ions by ALEs does not cause much fast ion loss to the wall, but rather the redistribution from the core to the peripheral region. This conclusion is consistent with the experimental result of the neutron emission profile measurement.

4.4 Discussion

When ALEs, which are the bursting modes with large amplitude in the range of TAE gap frequency, are occurred, total neutron emission rate decreases and neutral particle flux increases. The redistribution of fast ions was estimated from the change of the neutron emission profile measurement.

During Reversed-Shear-induced AE (RSAE) described in Sec. 4.1.4, transport of fast ions has been observed. RS deuterium discharges were performed for the study of fast ion transport by RSAE. Plasma parameters in these discharges were as follow: I_p= 0.9 MA, B_T= 2.1 T, P_{NNB} = 4.6 MW, E_{NNB} = 366.5 keV and $<\beta_h> \sim 0.4$ %. Since RSAE is sensitive to minimum of safety factor (q_{min}), in order to measure q-profile accurately toroidal field is relatively higher than the case of ALE. Figure 4.15 shows the experimental results: from the top, (a) beam injection power, (b) total neutron emission rate and (c) amplitude of magnetic fluctuation of the n =1 AE, where n is toroidal mode number. The suppression of total neutron emission rate was observed in the occurrence of n=1 RSAE. After n=1 RSAE disappeared, total neutron emission rate recovered about 20 %. Since the electron density and ion temperature did not changed from t = 5.8 s to 6.2 s, this suppression is considered due to fast ion transport. Figure 4.16(a) shows line integrated neutron emission rate at t = 5.8s during RSAE and at t = 6.2s after RSAE.

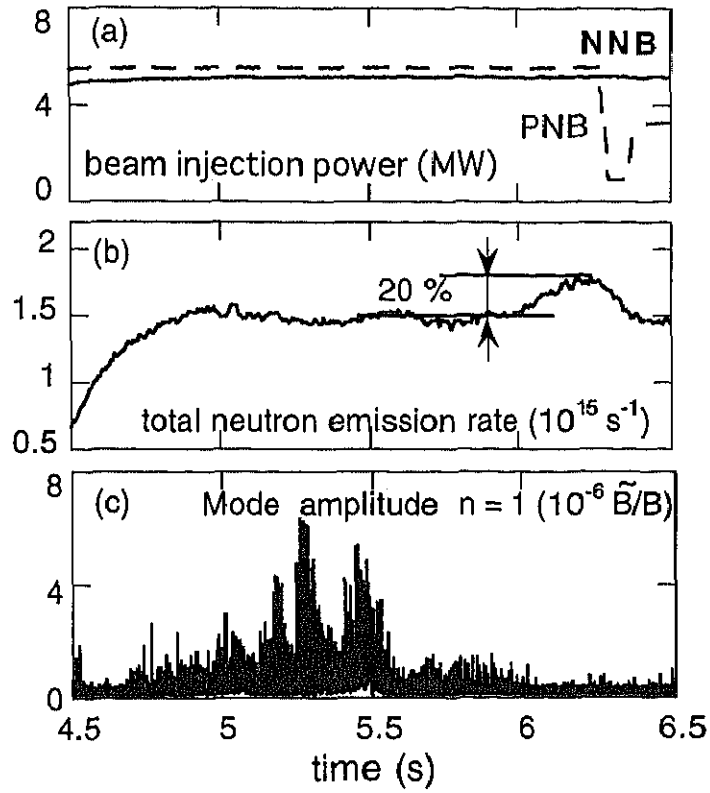

Figure 4.15 *Time trace of (a) beam injection power, (b) total neutron emission rate, (c) 0.1 ms averaged magnetic fluctuation of the n = 1 AE in E41449.*

Neutron emission rates in all channels are suppressed. Then, fast ion profile at t = 5.8 s and 6.2 s are estimated form measured neutron emission profile in the similar way in the case of ALEs. We can see that fast ions are loss in the whole plasma by RSAE as shown in Figure 4.16(b).

The result is different from the case of ALE redistributed of fast ions. This difference suggests transport of fast ions by AEs can explain by difference of eigenfunction of AEs in weak shear (WS) and RS plasmas. Fig.4.17 shows q-profile and the shear Alfvén continuous spectra versus r/a for (a) ALE at and (b) RSAE are shown. In the case of ALE, since magnetic shear is low in the center region, the eigenfunction seems to be localized in the center region. Because a low shear version of TAE can arise, called the *core localized mode* [34, 35] in such WS plasma and these core localized

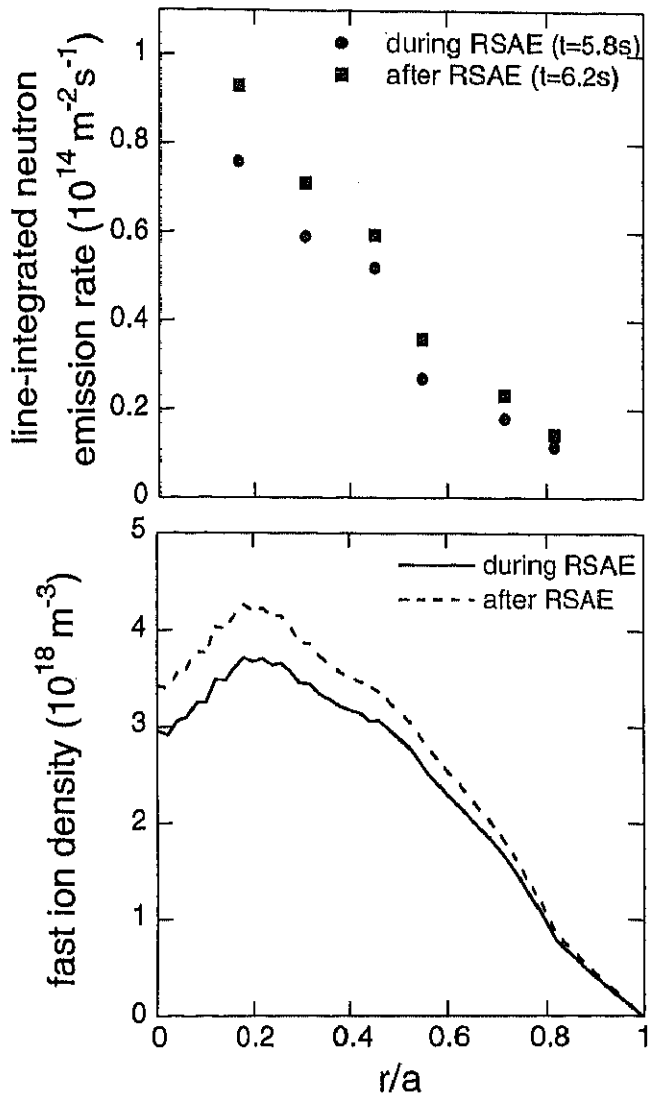

Figure 4.16 *(a) line-ingegrated neutron emission rate and (b) fast ion density profile estimated from neutron emission profile measuremet: at t = 5.8s during RSAE and at t = 6.2s after RSAE.*

modes can exist within a single Alfvén gap. As a result of the estimation of the change of fast ion distribution for all ALE during NNB injection in E39672, the averaged inversion point of fast ion profile by the redistribution is r/a ~ 0.44. Eigenfunction of RSAE is localized around q_{min}. From Fig.4.17(b), q_{min} is positioned at r/a ~ 0.4 and then eigenfunction of this mode exists around r/a ~ 0.4. Therefore, RSAEs can transport fast ions outer region in RS plasmas than ALEs.

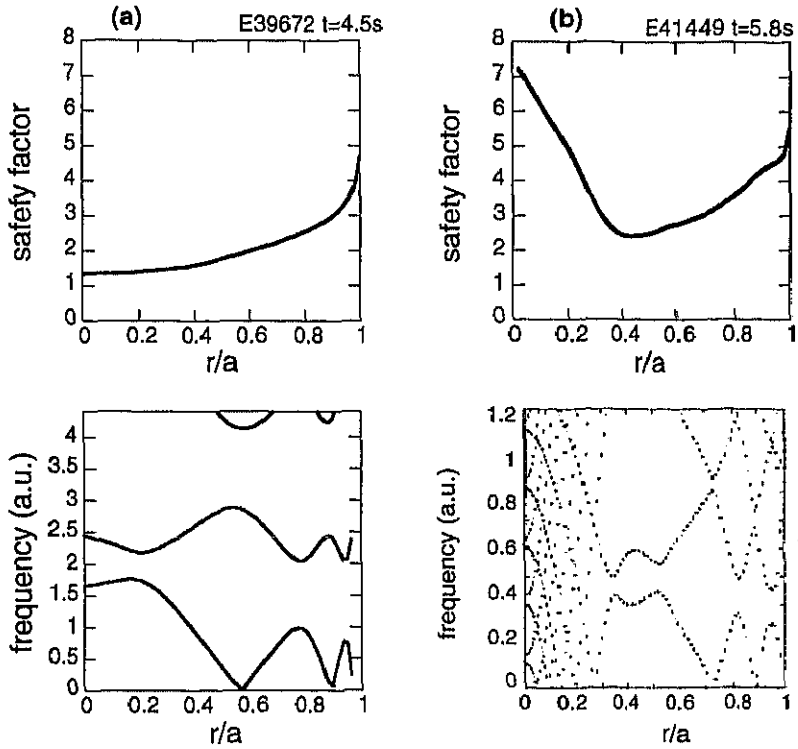

Figure 4.17 *Schematic drawing of the n=1 spectrum of AEs in the case of (a) ALE at t = 4.5 s in E39672, and (b) RSAE at t = 5.8 s in E41449.*

In the future, it is necessary to analyze the relation between the fast ion transport and eigenfunction of AEs more detail, together with the relation between the fast ion transport with mode amplitude. We will expect that the results of such as analysis give the useful knowledge in the operation scenario in ITER.

References

[1] D. J. Sigma, et al., Phys. Fluids B4 (1992) 1506)

[2] C. Z. Cheng, M. S. Chance., Phys. Fluids **29** (1986) 3695

[3] C. Z. Cheng, et al., Annals Phys. **161** (1985) 21

[4] W. W. Heidbrink, Plasma Phys. Control. Fusion **37** (1995) 937

[5] Y. Kusama, et al., Nucl Fusion **39** (1999) 1837

[6] K. Shinohara, et al., Nucl. Fusion. **41** (2001) 603

[7] M. Takechi, et al. submitted to Phys. Rev. Lett. (2002)

[8] Y. Kusama, M. Nemoto, V. I. Afanassie, et. al., Fusion Eng. Design **34-35** (1997) 531

[9] M. Ishikawa, et al., Accepted to Rev. Sci. Instru. (2002)

[10] L. C. Johonson, et al., Rev. Sci. Instru.**70** (1999) 1145

[11] J. M. Greene, et al., Phys. Fluids **14** (1971) 671

[12] H. L. Berk, et al., Phys. Fluids B4 (1992) 1806

[13] F. Zonca, L. Chen, Phys. Rev. Lett. **68** (1992) 592

[14] M. N. Rosenbluth, et al., Phys Rev. Lett. **68** (1992) 596

[15] M. N. Rosenbluth, et al., Phys. Fluids B4 (1992) 2189

[16] R. R. Mett, S. M. Mahajan, Phys. Fluids. B4 (1992) 2885

[17] R. Betti, J. P. Feidberg, Phys. Fluids. B4 (1992) 1465

[18] J. Candy, Plasma Phys. Control. Fusion **38** (1996) 795

[19] N. N. Gorelenkov, S. E. Sharapov, Phys. Scr. **45** (1992) 163

[20] G. Y. Fu, C. Z. Cheng, Phys. Fluids B4 (1992) 3722

[21] C. Z. Cheng, et al., in Plasma Physics and Controlled Nuclear Fusion Research 1992 (Proc. 14th Int. Conf. Fusion Energy, Wurzvurg, 1992) vol.2, IAEA, Vienna (1993) 51

[22] G. Y. Fu, et al., Phys. Rev. Lett. **75** (1995) 2336

[23] T. Ozeki, et al., Nucl. Fusion **35** (1995) 1553

[24] G. Y. Fu, et al. Nucl. Fusion **36** (1996) 1759

[25] M. Ishikawa, et al., submitted to Nucl. Fusion (2002)

[26] T. Hatae et al., Rev. Sci. Instrum. **70** (1999) 772

[27] Y. Koide, et al., Rev. Sci. Instrum. **72**, 119 (2001)

[28] T. Nishitani, et al., Rev. Sci. Instru. **63** (1992) 5270

[29] H. Shirai, et al., J. Phys. Soc. Jpn, **64**, (1995) 4209

[30] Y. Yamashita, JAERI-M **87**-206 (1998)

[31] D. R. Mikkelsen Nucl. Fusion **29** (1989) 1113

[32] H. S, Bosh et al., Nucl. Fusion **32** (1992) 611

[33] T. H. Stix, Plasma phys. **14** (1072) 367

[34] R. B. White et.al. Phys. Fluids **26** (1983) 2958

[35] G. Y. Fu, Phys. Plasmas **2** (1995) 1029